2012년 2월

석사학위논문

Segmentation and Analysis of Red Blood Cells by Digital Holographic Microscopy

조선대학교 대학원

컴 퓨 터 공 학 과

역 발 류

디지털 홀로그램 현미경에 의한 적혈구 자동 추출 및 분석

Segmentation and Analysis of Red Blood Cells by Digital Holographic Microscopy

2012년 2월 24일

조선대학교 대학원

컴 퓨 터 공 학 과

역 발 류

디지털 홀로그램 현미경에 의한 적혈구 자동 추출 및 분석

지도교수 문 인 규

이 논문을 공학 석사학위신청 논문으로 제출함

2011년 10 월

조선대학교 대학원

컴 퓨 터 공 학 과

역 발 류

역발류의 석사학위논문을 인준함

위 원 장　조선대학교 교수　정 일 용 (인)

위　　원　조선대학교 교수　문 인 규 (인)

위　　원　조선대학교 교수　이 상 웅 (인)

2011년 11 월

조선대학교 대학원

Contents

LIST OF FIGURES

ABSTRACT

Segmentation and Analysis of Red Blood Cells by Digital Hologrphic Microscopy

Faliu Yi

Advisor : Prof. Inkyu Moon, Ph.D.

Department of Computer Science

Graduate School of Chosun University

In this thesis, we have applied the marker-controlled watershed algorithm to achieve automated segmentation of the red blood cells(RBCs) phase images. The phase image of RBCs is obtained by using off-axis digital holographic microscopy. In order to calculate a correct phase value of RBC and analyze it quantitatively, it is important to perform a background subtraction of the phase images and set 0° value to the background parts of the RBCs phase image for the purpose of comparing the RBCs phase image. The most important process of segmentation based on marker-controlled watershed is achieving an accurate locatization of internal and external markers. Here, we first obtain the binary image via Ostu algorithm. Then, we apply the

morphological operation to the binary image to get the internal markers, and we use the distance transform combined with the watershed algorithm to generate external markers based on internal markers. Finally, combining the internal and external markers, we modify the original gradient image and apply the watershed algorithm to them. By appropriately identifying the internal and external markers, the problems of over-segmentation and under-segmentation are avoided. Furthermore, the inside and outside parts of RBCs phase image can also be segmented by using the marker-controlled watershed combined with our method which can identify the internal and external markers appropriately. Our experimental result shows that the proposed procedure achieves good performance in terms of segmenting RBCs. After segmentation, the properties of RBCs such as mean phase value, projected surface area, dry mass and sphericity coefficient can be obtained and analyzed in deatil.

1. Introduction

Three-dimensional (3D) image processing techniques have received increased attention with the development of the 3D optical imaging system [1-12]. It becomes easier and more convenient to obtain the computational 3D image of objects [6]. Thus, 3D digital image processing, which can directly affect future research on the object under study, becomes more important. Recently, 3D image processing of holographic images has played an important role in the segmentation, recognition, and tracking of macro or micro objects [13-15]. However, due to the noises in the computational holographic image, some blurs will occur in the background of the image. Therefore, the processing of holographic image segmentation [16] is inevitable. Since most image segmentation methods are time-consuming and inaccurate, the automated and accurate holographic image segmentation is strongly needed.

Red blood cells (RBCs) are being extensively studied for many bio-medical applications [17, 18]. The RBCs, which are an imperative element of human blood, play an essential role in human health. Automated 3D imaging and segmentation of RBCs may be helpful for identifying different kinds of RBCs or various blood diseases involving RBCs. Therefore, it is very important to perform a background subtraction of phase images in order to calculate a correct phase value of RBC, which allows for quantitative measurement of characteristic properties such as dry mass, cell surface, and density, sphericity coefficient, volume and the mean phase of RBCs. Furthermore, the segmented phase image of RBCs also benefits the tracking of single or multiple RBCs for their dynamics (3D morphology and biomass changes) analysis.

Since most single RBCs have two different characteristics (the inside part is different from the outside one), it is better to separate those different parts, respectively, in order to comprehensively analyze RBCs in detail.

Thus, segmenting the inside and outside parts is also significant.

Segmentation is to partition an image into several regions where it has similar characteristic such as similar color, intensity value or texture. Segmentation approaches can be broadly classified into four categories [19, 20]. The first category is threshold-based segmentation. It is the simplest, easiest and fastest method. The problem of this approach is that it is not easy to find an appropriate threshold. The second one is region-based segmentation which include region growing and region splitting and merging methods. However, it is difficult to find an appropriate stop criteria for these region-based methods. The third one is edge-based segmentation. This method need the change of intensity value between needed object and background to be distinct. Moreover, it is often produce false edges. The forth category is watershed based segmentation. It uses both edge and region information to segment the image. The disadvantage of this method is over-segmentation problem.

For the RBCs phase image, some of the parts in the single RBC reconstructed by using the off-axis digital holographic microscopy have similar phase values as the background. This is shown in Fig. 1(a). So, it is not easy to segment the phase image only with threshold-based or region-based algorithms. The other problem is that most single RBCs have two gradients. One gradient is between a RBC and background, while the other is within the single RBC as shown in Fig.1(b) and (c).This makes it difficult to segment the cells only based on edge. Due to the gradient within the RBC, inaccurate segmentation is always generated. Furthermore, some of the RBCs are connected to each other as shown in Fig. 1(d). This can also affect the segmentation of isolated RBC. All of these problems complicate the phase image segmentation of RBCs.

In this paper, we use the marker-controlled watershed algorithm to segment the RBCs phase image that is reconstructed from the hologram image obtained by off-axis digital holographic microscopy [21-25]. Specially, our automated

RBC segmentation method can be suitable for the quantitative comparison of different types of RBCs since the phase values in the background parts of the RBCs phase image can be set to zero value.

First, Otsu algorithm [20] is applied to obtain the binary image. Then, a morphology operation is conducted on the binary image. After a series of morphology operations such as morphological opening, erosion and reconstruction, we can get the proper internal markers of these cells, which can avoid the effect of internal gradient and connection among different cells. With the internal markers, we generate the external markers by using the distance transform algorithm combined with the watershed algorithm [20]. Finally, we can apply the watershed algorithm to the modified gradient image obtained by the minima imposition technique [26] with the extracted internal and external markers. With these methods, good experimental results are obtained.

This paper is organized as follows. In section 2, the digital holographic microscopy is described. In section 3, we briefly describe the principle of morphological operation and watershed transform algorithm. In section 4, the procedure of the proposed method for RBCs segmentation and analysis is presented. Then, in section 5, we show the experimental results. Finally, we conclude this paper in section 6.

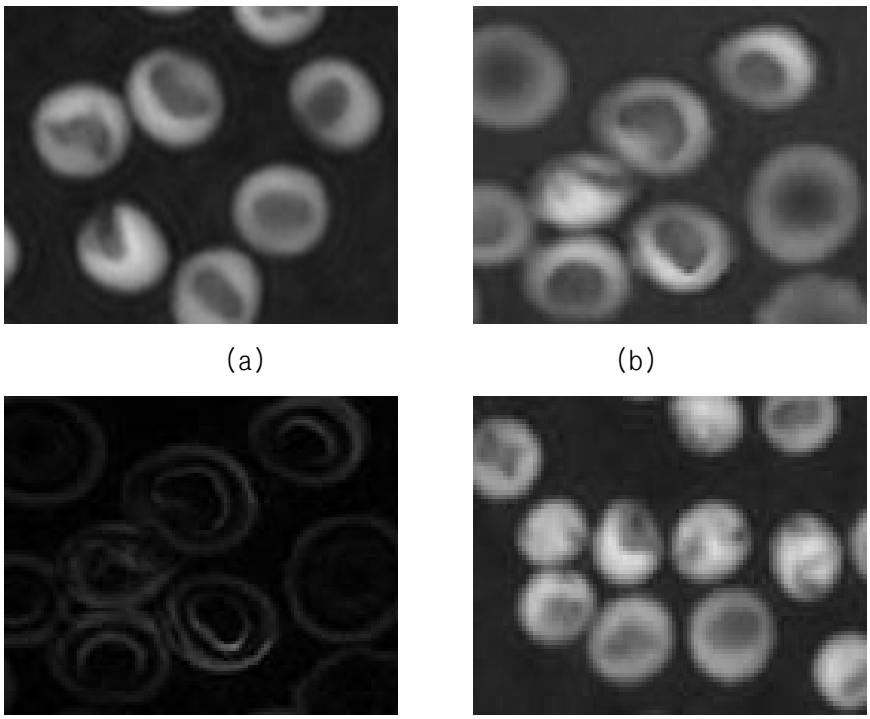

Figure 1. Some characteristics of red blood cells phase image.

In figure 1, (a) shows that some of the parts in the single RBC have similar phase value as the background. (b) is the original RBCs phase image which has two kinds of edges (inside and outside parts). (c) is the gradient image of (b). (d) shows that some of the RBCs are connected to each other.

2. Digital holographic microscopy

Due to the semitransparent of RBCs, 2D RBCs image can not provide detail information about RBCs such as cell structure and biomass. In this paper, the off-axis digital holographic microscopy is applied to capture the 3D RBCs because of its low-cost, noninvasive and fast. Figure 2 shows the schematic of off-axis digital holographic microscopy. We use the off-axis digital holographic imaging system which has been described in [21]. Holograms are acquired with a transmission digital holographic microscopy (DHM) setup as shown in Fig. 2. The experimental setup is a modified MachZehnder configuration with a laser diode source (λ= 683 nm). The laser beam is divided into a reference wave and an object wave. The object wave is diffracted by the RBC samples, magnified by a 40×/0.75NA microscope objective and interferes, in the off-axis geometry, with the reference wave to produce the hologram recorded by the CCD camera. The reconstruction and aberration compensation of the RBC wavefront is obtained by using the numerical algorithm described in [22, 23].

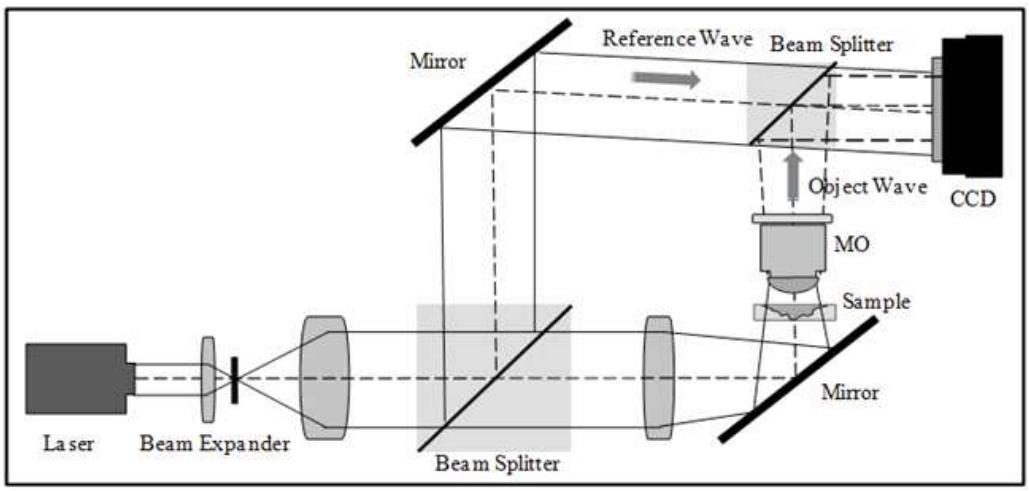

Figure. 2. Schematic of the off-axis digital holographic microscopy.

3. Morphological Operation and Watershed Transform Algorithm

In our segmentation method, the widely used algorithms consist of morphological operation and watershed transform. In this section, the basic concept of morphological dilation, erosion, opening and closing will be described. In addition, the knowledge of watershed transform and marker-controlled watershed will also be given.

3.1 Morphological Operation

3.1.1 Morphological Dilation and Erosion

Morphological dilation is to extend or thicken the target in an image. The level of extension or thickness for the target is controlled by a moving window called structuring element. The effect of morphological dilation is illustrated in figure 3 with binary image.

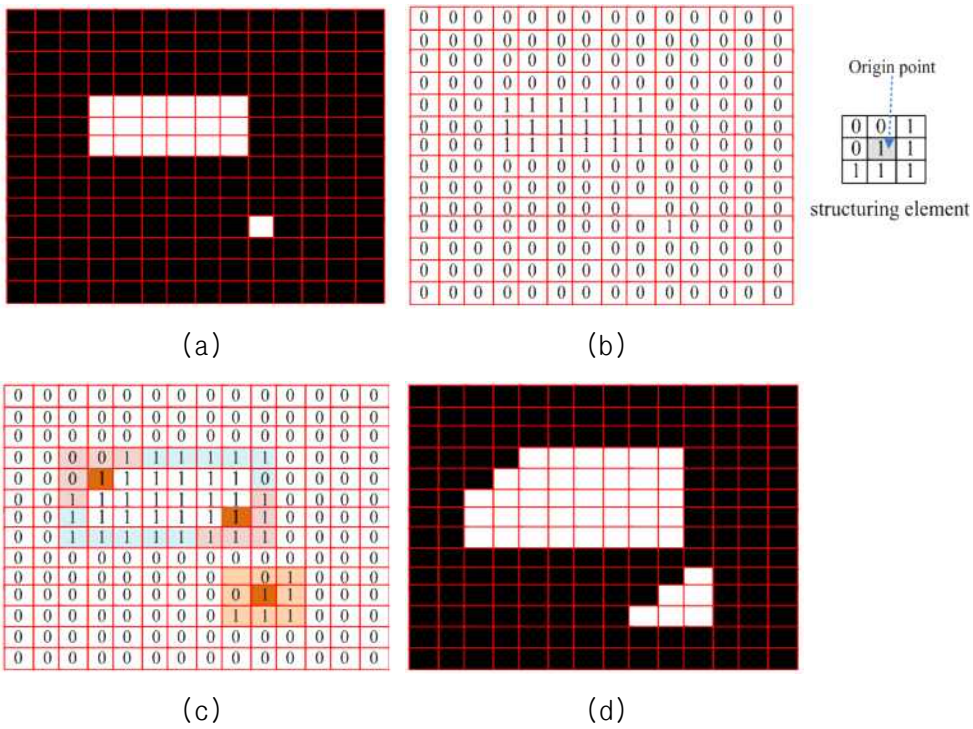

Figure 3. Illustration of morphological dilation

In figure 3, (a) is the original binary image, (b) is the corresponding pixel value of original binary image and the structuring element,(c) is the pixel value of image after morphological dilation with structuring element in (b) and (d) is the corresponding displayed image after morphological dilation.

Just as showed in figure 3, the origin point of the structuring element has to be translated in the image in order to overlap every pixel in the original image. When the origin point of structuring element and its overlapped point in the image is the same, the overlapped points in the image will be extended as the 1-values in structuring element. The morphological dilation can be defined as following set operation:

$$A \oplus B = z | (\hat{B})_z \cap A = \varnothing \qquad (1)$$

where A is original image, B is the structuring element, $\oplus$ is the symbol of

dilation, $\hat{B}$ is the reflection of set B, and $(\hat{B})_z$ is the translation of $\hat{B}$ by point z that are the output points.

Morphological erosion is the opposite operation of dilation. Erosion can shrink the objects in an image. The erosion degree is also controlled by a structuring element. The erosion process is presented in figure 4.

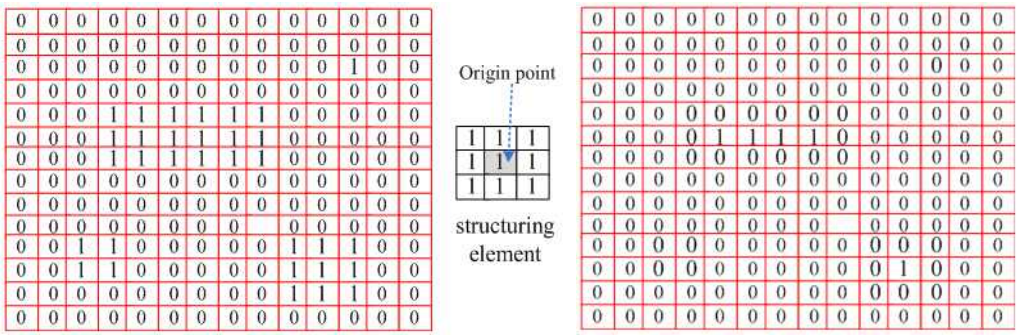

(a) (b)

Figure 4. Illustration of morphological erosion

where (a) is the original binary image and structuring element while (b) is the binary image after erosion by structuring element in (a).

For morphological erosion, the structuring element will be translated throughout the original image. When the structuring element totally fits the overlapped points in the image, the point in the image that overlaps the origin point in the structuring element will be kept as point in the output image. The erosion process can be expressed as following set operation:

$$A \ominus B = z | (B)_z \subseteq A \qquad (2)$$

where A is the original image, $\ominus$ denotes erosion operation, and B is the structuring element, z is the output points and $(B)_z$ is the translation of B at point z.

3.1.2 Morphological Opening and Closing

Morphological opening and closing are the combination of morphological dilation and erosion. Morphological opening is defined as a morphological erosion followed by a dilation. The morphological A by B where A is original image and B is structuring element are represented as following equation:

$$A \circ B = (A \ominus B) \oplus B \tag{3}$$

where $\circ$ denote opening operation, $\ominus$ is morphological erosion and $\oplus$ is morphological dilation. The effect of morphological opening is to remove region in the image that can not entirely contain the structuring element when structuring element translate within the image. This operation can smooth the object edge. Figure 5 is the illustration of morphological opening.

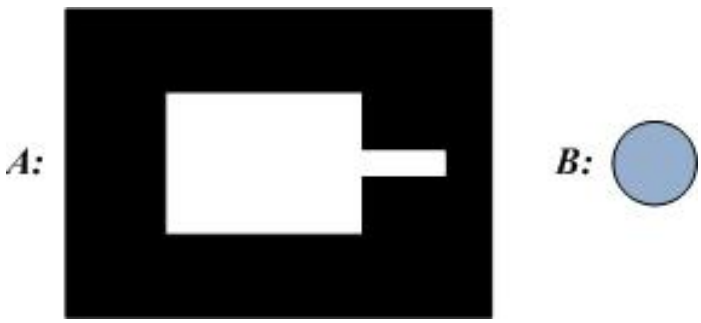

(a)

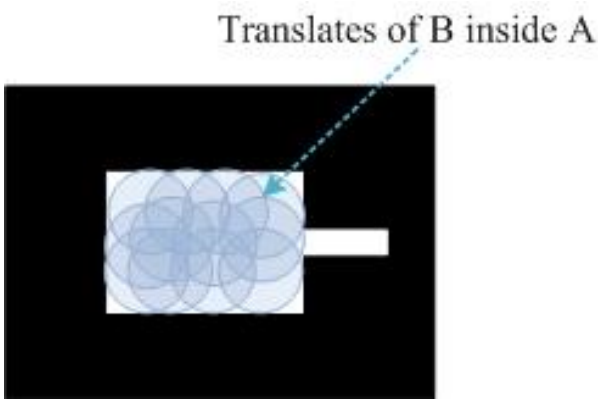

(b)

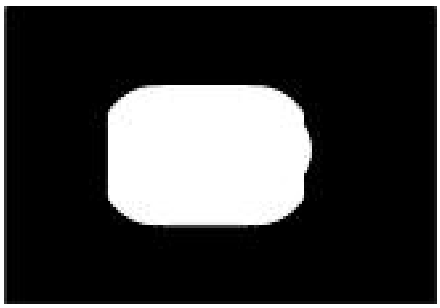

(c)

Figure 5. illustration of morphological opening

where (a) is the original image and disk shape structuring element. (b) is the illustration of structuring element translated inside A while (c) is the morphological opening result.

Morphological closing is the opposite operation of opening. It is defined as a morphological dilation following by an erosion. The morphological closing of A by B can be written as:

$$A \bullet B = (A \oplus B) \ominus B \tag{4}$$

where • denotes morphological closing operation, $\oplus$ is morphological dilation and $\ominus$ is morphological erosion. Morphological closing can also smooth the contours and it can achieve connecting narrow breaks, filling holes and thin gulfs which are smaller than the structuring element. The effect of morphological closing is illustrated in figure 6.

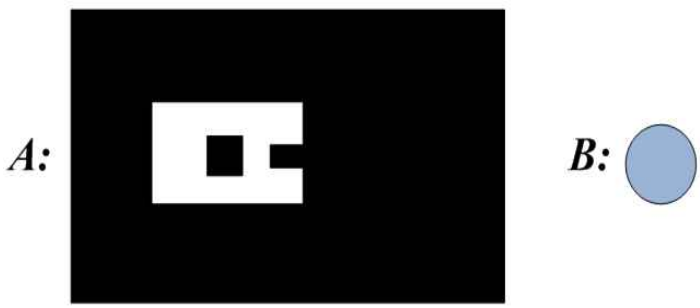

(a)

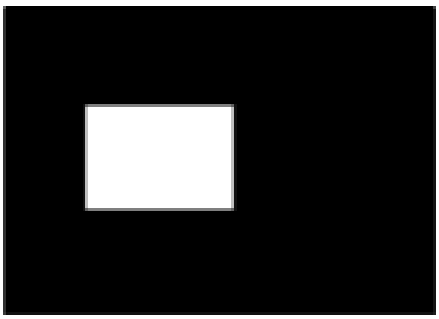

(b)

Figure 6. illustration of morphological closing

where (a) is image A and disk shape structuring element B and (b) is morphological closing result of A by B.

3.1.3 Morphological Reconstruction and Filling

Morphological reconstruction is the combination of dilation and sets intersection operations. It includes two images and one structuring element. One image is the original image called mask and the other one is marker image which consists of marked points. The structuring element is a 3 by 3 matrix with values of 1s. The morphological reconstruction method can be described as following steps:

Step 1: choose mask image A and marker image M.

Step 2: do the following operation:

$$M_{k+1} = (M_k \oplus B) \cap A \tag{5}$$

until M_{k+1} equals M_k where B is structuring element of 3 by 3 with values of 1s and $\oplus$ is morphological dilation operation. M_{k+1} is the output of reconstructed image. The morphological reconstruction can be expressed as term like:

$$R_A(M) \tag{6}$$

where R means morphological reconstruction, M is a marker image and A is a

mask image. The effect of morphological reconstruction is illustrated in figure 7.

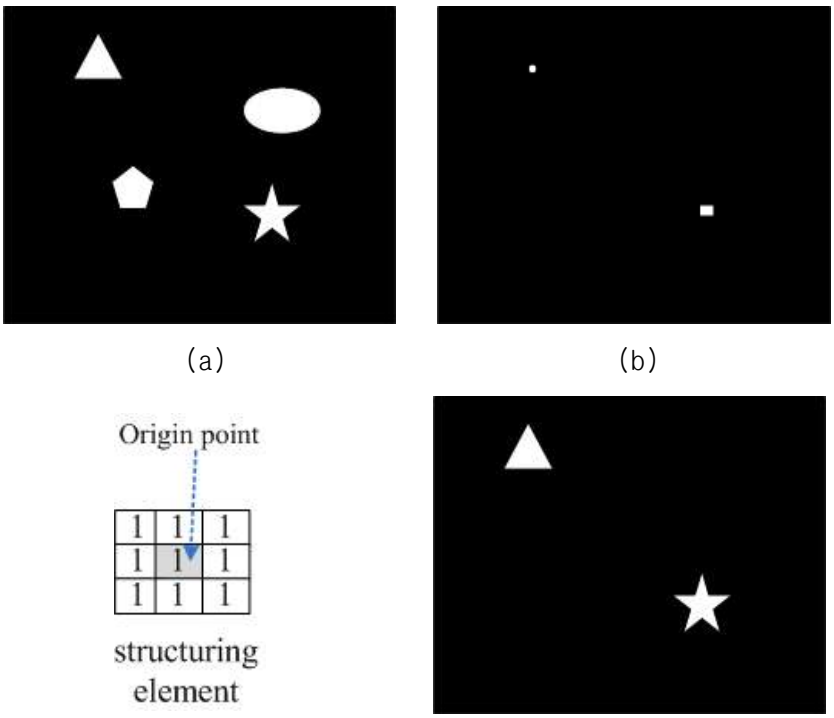

Figure 7. Illustration of morphological reconstruction

where (a) is the mask image (original binary image) and (b) is the marker image, (c) is a 3 by 3 structuring element with values of 1 and (d) is the reconstructed image after morphological reconstruction operation.The marker image in morphological reconstruction should be the subset of mask image in order to reconstruct the component in mask image.

The function of morphological filling is to fill the holes in a binary image. It is the application of morphological reconstruction by choosing appropriate mask and marker image. For the morphological filling operation, the mask is defined as the complement of original binary image and the maker is selected as the image where the pixel values at the border are set to be

the subtracted value of 1 with the original pixel value while values in other pixels are 0s. This can be represented as following equation:

$$M(x,y) = \begin{cases} 1 - A(x,y) & (x,y): \ border of \ A \\ 0 & other locations \end{cases} \quad (7)$$

The output image F after morphological filling is defined as the complement of image obtained by morphological reconstruction where the complement of original binary image A is used as mask image and M described in eq.(6) as marker image. F can be expressed as:

$$F = [R_{A^c}(M)]^c \quad (8)$$

The effect of morphological filling operation is illustrated in figure 8.

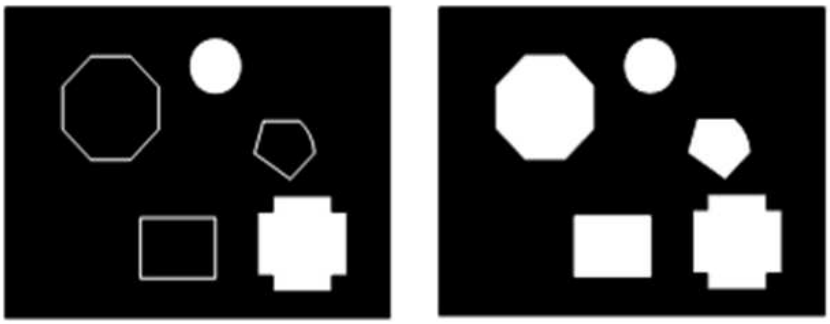

(a) (b)

Figure. 8. Illustration of morphological filling

where (a) is the original binary image with holes for some objects and (b) is the image after morphological filling operation

3.2 Marker-Controlled Watershed Transform Algorithm

The watershed transform algorithm has the advantage of generating closed boundary of the needed objects [27]. Moreover, the execution speed is also acceptable. However, the problem is that the watershed algorithm easily leads to over-segmentation. The marker-controlled watershed algorithm, which

is the extension of watershed transform algorithm, offers a way to reduce the over-segmentation problem. In this section, both the watershed and marker-controlled watershed algorithms will be reviewed.

3.2.1 Watershed Transform

The watershed transform algorithm is based on flooding simulation. In this algorithm, we can imagine the image as terrain and the intensity value as height. Taking the regional minima values in the image as valleys and the regional maxima values as peaks, when water floods this terrain, dams are built among different valleys. Watershed transform finds the peak values between every two valleys as shown in Figure 9. These peaks form the watershed line.

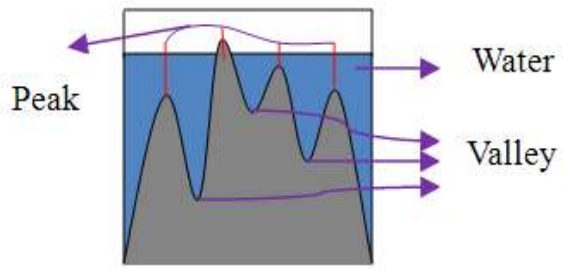

Figure 9. Flooding simulation model of watershed transform algorithm

In Meyer's algorithm [28], watershed transform is implemented. First, a set of markers are chosen as valleys and each of them is given a different label. Then, put all of the neighboring pixels of each labeled area into a priority queue with a priority level, which is the intensity value. After that, the highest priority is picked from the priority queue. If the picked value's neighbors, which are already labeled, have the same label, then this picked value is labeled with the same label as the label area. At the same time, all non-labeled neighbors are inserted into the priority queue. This step is repeated until the priority queue is empty. Finally, the

non-labeled intensity values are the peak values (see Fig. 9) that are included in the watershed lines.

3.2.2 Marker-Controlled Watershed Transform

In the watershed transform algorithm, water floods the terrain from the regional minimum value. However, marker-controlled watershed floods the terrain according to the markers value and finds the maximum values between every two markers. These maximum values are the watershed lines. In marker-controlled watershed, there are internal and external markers. Internal markers represent the objects that we want to obtain. So, if we want to get the correct objects, then we should mark all objects as internal markers. Conventionally, the internal markers are obtained by a threshold algorithm. On the other hand, the external markers represent the background around the objects. A better way to obtain external markers is by using Distance Transform combined with watershed algorithm based on internal markers. Distance transform is the distance from every pixel to the nearest nonzero-valued pixel [20].

Usually, watershed transform is applied to a gradient image because the objects and background commonly correspond to a low value, while the edge corresponds to a high value in the gradient image. Unfortunately, due to noise and other local irregularities of the gradient image, it always contains a large number of regional minima values. So, the segmentation result is not correct. In marker-controlled watershed, after the internal and external markers are obtained, they are used to modify the gradient image. Through minima imposition technique [26], only the positions, which are the locations of the markers value, become regional minimal values. Thus, the extra unnecessary regional minimal values can be removed. Then, we can apply the watershed transform algorithm to this modified gradient image. The effect of marker-controlled watershed segmentation is shown in Figure 10.

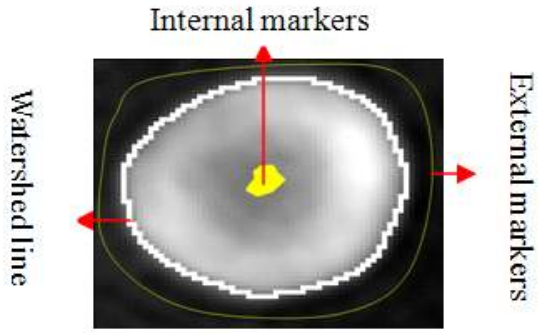

Figure 10. illustration of marker-controlled watershed algorithm

4. Red Blood Cells Segmentation and quantitative Analysis

4.1 Procedure of RBCs Segmentation

Although the existing marker-controlled watershed described in [20] provides a better way to reduce over-segmentation, it cannot efficiently extract the internal and external markers. Thus, we present a method that can efficiently extract the markers in the phase image of RBCs and achieve good segmentation result based on marker-controlled watershed. By using this method, we can solve the problems presented in Fig. 1. Furthermore, under-segmentation can also be avoided properly. The steps of this improved marker-controlled watershed of the RBCs phase image segmentation are described as follows:

Step 1: Normalize the phase image of RBCs. Denote as I_{nom}.

Step 2: Segment I_{nom} by using Otsu's method [20] and fill the holes by morphological reconstruction [20]. Denote as I_{bin}.The Otsu's method can be implemented as the following equation:

$$\sigma^2(t) = \omega_1(t)\omega_2(t)[\mu_1(t) - \mu_2(t)]^2 \tag{9}$$

where $\sigma^2(t)$ is the variance of the inter-class, $\omega_i(t)$ and $\mu_i(t)$ are the class probability and class means, respectively. The variable t which can maximize the inter-class variance $\sigma^2(t)$ is the desired threshold.

Step 3: Obtain the gradient magnitude of the original phase image. Denote as I_{grad}. Here, sober operator was used to calculate the gradient on both vertical and horizontal direction which can be described as follows:

$$g_x = \begin{bmatrix} -1 & 0 & 1 \\ -2 & 0 & 2 \\ -1 & 0 & 1 \end{bmatrix} * I_{bin} \quad \text{and } g_y = \begin{bmatrix} -1 & -2 & -1 \\ 0 & 0 & 0 \\ 1 & 2 & 1 \end{bmatrix} * I_{bin} \tag{10}$$

$$I_{grad} = \sqrt{(g_x^2 + g_y^2)} \tag{11}$$

where I_{grad} is the image of gradient magnitude, I_{bin} and * is source image, symbol of convolution operation respectively.

Step 4:Obtain the internal markers.

a: Do morphological opening operation [20] to I_{bin} with a disk structuring element whose radius is 9 and denoted as I_{open1}. This disk structuring is much smaller than the smallest RBC so as to preserve all needed objects while simultaneously removing the additional noise.

b: Do morphology erosion operation to I_{ero1} by a disk structuring element with a radius of 17. Get image I_{ero1}.This disk structuring is approximately medium sized relative to the size of RBC. This process aims to separate the connected objects.

c: Take image I_{ero1} as marker and image I_{open1} as mask, do the morphological reconstruction operation to them. The obtained image is denoted as I_{rec1}.

d: Subtract image I_{rec1} from image I_{open1}. Obtain image I_{sma1}.In the case shown in Fig.10, when we want to separate the connected cells in Fig.11(a), we use a disk structuring element with a radius of 17 as described in step 4.a to erode this image. However, this will totally erode the small RBC as shown in Fig. 11(b). Thus, without further operation, it will bring on under-segmentation. Most small will disappear. So, the purpose of this step is to get back these cells with small size.

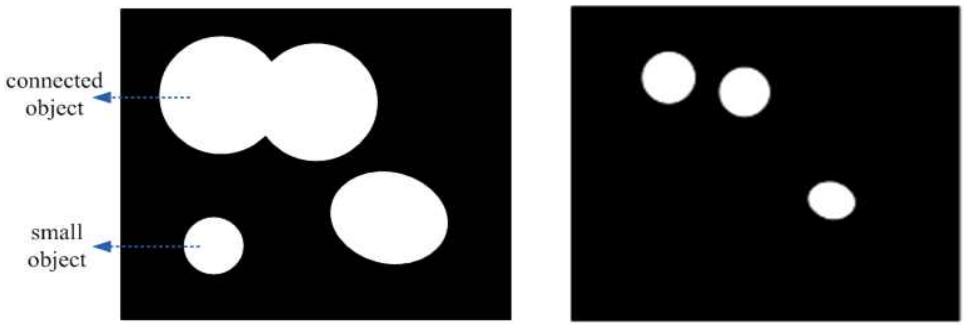

(a) (b)

Figure 11. erosion of the connected RBCs and small RBCs.

in figure 11, (a) denote the phase image having connected and small RBCs, (b) is the erosion result of image (a) with big disk structuring element and the smaller object will disappear.

e: Do the morphological dilation operation to image I_{ero1} by a disk structuring element with a radius of 11. This step can reduce the effect of internal gradient as described in Fig. 1(b) since it can expand the center area which will cover the location of internal gradient. We denote the image of this step as I_{dila}.

f: Combine image I_{sma1} in step 4.d with image I_{dila} in step 4.e ; the result, which has marked most of the objects, can be used as internal markers. We denote this image as I_{inter}.

Step 5: Obtain the external markers by image I_{inter} in step 4.e using the distance transform algorithm and watershed transform. This image is denoted as I_{exter}.The distance transform of a binary image, which is the distance from every pixel to the nearest nonzero-valued one, can be expressed as:

$$\begin{cases} D(x_i,y_i)=0 & \text{if } O(x_i,y_i)=1 \\ D(x_i,y_i)=\sqrt{(x_i-x_j)^2+(y_i-y_j)^2} & \text{if } O(x_i,y_i)=0 \end{cases} \quad (12)$$

where $D(x,y)$ is the distance transform image, $O(x,y)$ is the source image and $O(x_j,y_j)$ is the nearest non-zero value pixel of $O(x_i,y_i)$.

Step 6: Combine the internal markers I_{inter} with external markers I_{inter}.We

get the final markers image I_{mark}.Then, we can modify the gradient magnitude image I_{grad} obtained in step 3 by using the minima imposition technique [26], which can be described as [29]:

$$I_{\mathrm{mod}ify} = R^{\varepsilon(I_{grad}+1)\wedge I_{mark}}(I_{mark}) \tag{13}$$

Finally, the watershed transform algorithm is applied to modified gradient image $I_{\mathrm{mod}ify}$. We can get the reasonable segmented phase image I_{obj}.

Figure 12 is the flow chart of the proposed method. In this improved marker-controlled watershed, we can efficiently and correctly extract the internal and external markers. It also has the advantage of reducing the problem of over-segmentation and under-segmentation.

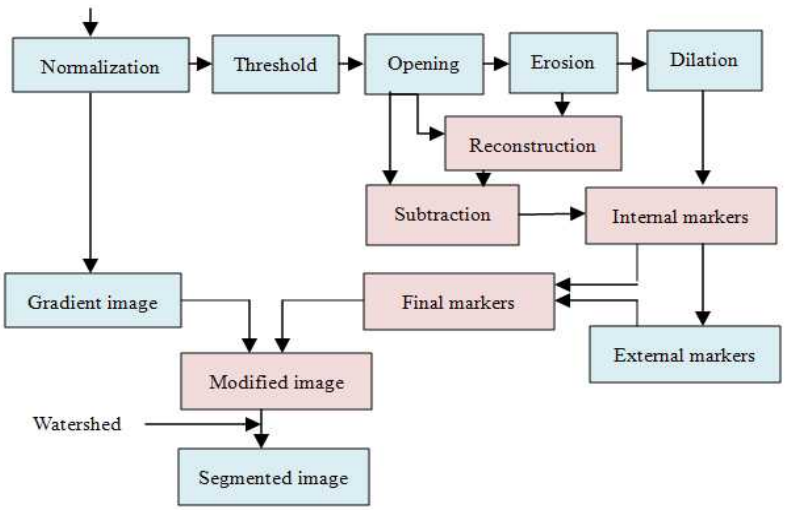

Figure 12.Flowchart of the proposed phase image segmentation method

After obtaining the segmented RBCs, the next step is to segment the inside and outside parts of RBCs based on the segmented phase image I_{obj}.The segmentation procedure of these two parts can be described as follows.

Step 1: get the gradient image (using Sobel operation on both vertical and horizontal direction) and binary mask image of I_{obj}.We denote them with I_{grad2}

and I_{bin} , respectively.

Step 2: obtain external markers:

Erode the binary mask image I_{obj} by a disk structuring element with radiuses of 5 and 7 respectively. Get images I_{erod1} and I_{erod2}.Do the complement operation to I_{erod1} and I_{erod2},the obtained images can be denoted with I_{comp1} and I_{comp2}. The image $I_{comp1}$is the needed external markers denoted as I_{exter2}.

Step 3: obtain internal markers:

a: multiply I_{obj} by I_{erod2},add the resulted image with I_{comp2}.Get the image I_{add}.

b: segment I_{add} with the threshold method(threshold is set to 0.45). Denote the segmented image as I_{thre1}.

c: obtain the internal markers I_{inter2} by doing the morphology close operation to the complemented image of I_{thre1} with a disk structuring element whose radius is 5.

Step 4: get the new markers I_{mark2} by combining the internal markers I_{inter2} and external markers I_{exter2}.

Step 5: modify the gradient phase image I_{grad2} with I_{mark2} via the minima imposition technique. Get image $I_{modify2}$.

Step 6: obtain the inside part of RBCs image I_{inside} by applying the watershed algorithm to $I_{modify2}$.

Step 7: obtain the outside part of RBCs image $I_{outside}$ by subtracting I_{inside} from I_{obj}.

4.2 Red Blood Cells Analysis

After the segmentation, every single RBC can be extracted. Then, the RBC's properties such as Mean phase value, Area, Dry Mass and sphericity coefficient can be obtained. The following subsections are the definition of

these properties used for RBCs analysis.

4.2.1 Mean Phase Value and Area

The surface area and mean of phase values are calculated by using the following equations, respectively.

$$S = Np^2,\ \bar{\varphi} = \frac{1}{N}\sum_{i=1}^{N} x_i \tag{14}$$

where N is the total number of pixels within single RBC, p denotes the pixel size, and x_i is the phase value at the ith pixel within the single cell.

4.2.2 Dry Mass

The dry mass (DM) is the weight of the cell when completely dried, which is usually considered as a reliable measure of the biomass. The DM is defined as the following equation [24]:

$$Dry\,Mass\,(DM) = \frac{10\lambda}{2\pi\alpha}\int_s \varphi ds = \frac{10\lambda}{2\pi\alpha}\bar{\varphi} S \tag{15}$$

where λ is the wavelength of the light source, α is a constant, and the value can be approximated to be $0.002 m^3/kg$. It is noted that DM is proportional to the surface area, S, and the averaged phase value, $\bar{\varphi}$.

4.2.3 Sphericity Coefficient

The sphericity coefficient is defined as a ratio of thickness at the center of RBC to the thickness at quarter of its diameter. Since the thickness of RBC is reflected by the phase value, sphericity coefficient can be alternatively calculated by phase value at the center of RBC and that at quarter of its diameter. Usually, there are three morphological types of RBC which are biconcave disk, flat disk, and spherocytes. Different types of RBC have different functionality in terms of oxygen transfer. Sphericity coefficient k as a morphological measurement is effective to differentiate

these types of RBCs and can be expressed as following equation:

$$k = \frac{ph_c}{ph_d} \tag{16}$$

where ph_c and ph_d are phase value at the center of RBC and quarter of its diameter respectively.

5. Experimental Results

5.1 Red Blood Cells Segmentation Result

In this experiment, the phase image of RBCs is reconstructed from their digital hologram which is recorded by using off-axis digital holography microscopy. Here, we will use two kinds of RBCs to illustrate the robustness of our method (more than 100 images are tested). One is newer RBCs with a 14-day storage period, while the other is older RBCs with a 38-day storage period. In Fig.13, the segmented images using classical watershed and marker-controlled watershed described in [20] are presented.

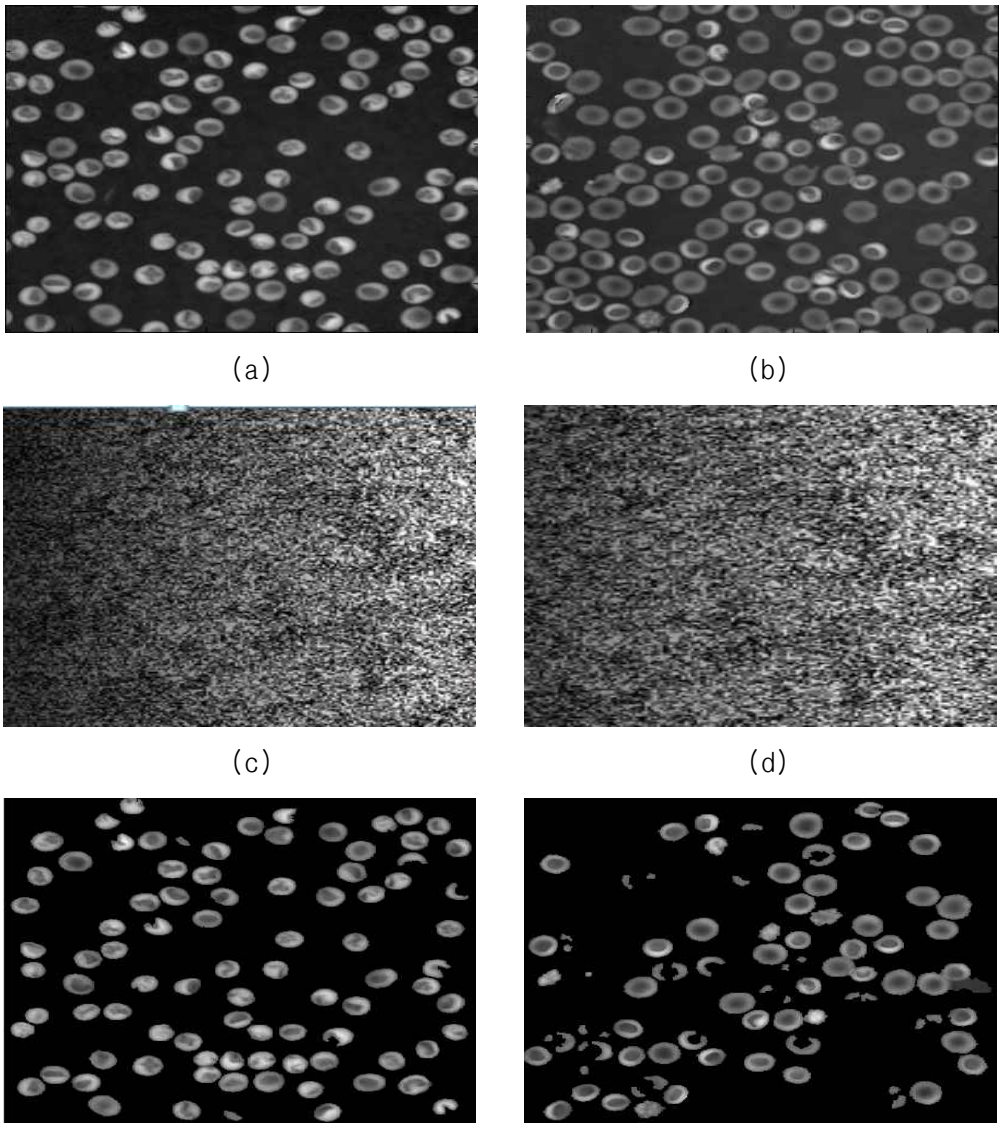

Figure .13 segmentation results with classical watershed and marker-controlled watershed algorithm directly.

In figure 13, (a) and (b) are the original RBCs phase image while (a) is newer RBCs and (b) is older RBCs, (c) and (d) are the corresponding

segmentation result via classical watershed while (e) and (f) are the corresponding segmentation result via classical marker-controlled watershed.

From the results in Figure.13, we can conclude that the conventional watershed and marker-controlled watershed without further processing cannot achieve a correct segmentation effect. Problems such as over-segmentation, under-segmentation and touched cells cannot be solved properly.

In the following, we will present the experimental result of using our improved marker-controlled watershed that can properly extract the internal and external markers. Figure 14 shows the result of the key steps of our segmentation process.

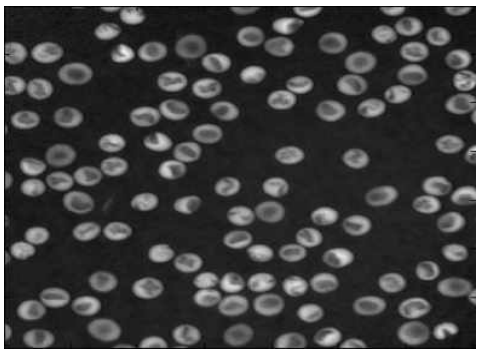

(a)

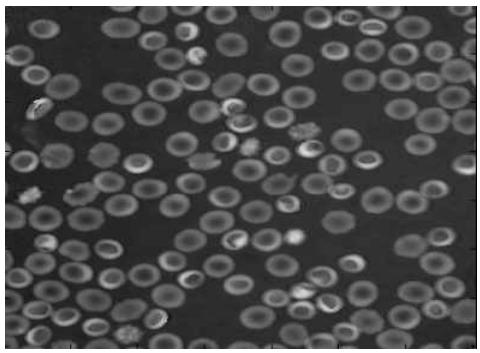

(b)

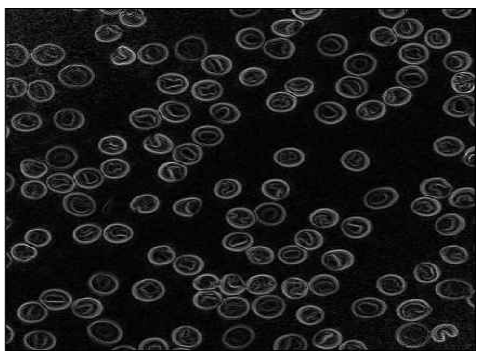

(c)

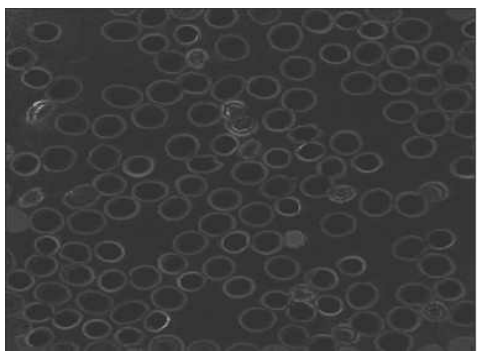

(d)

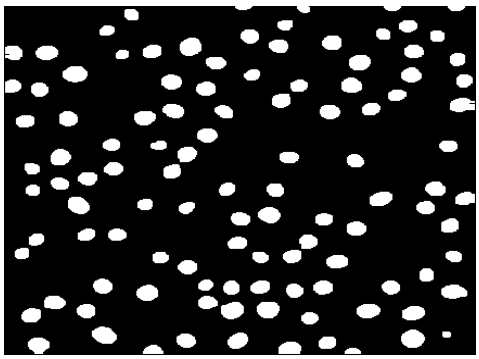

(e)

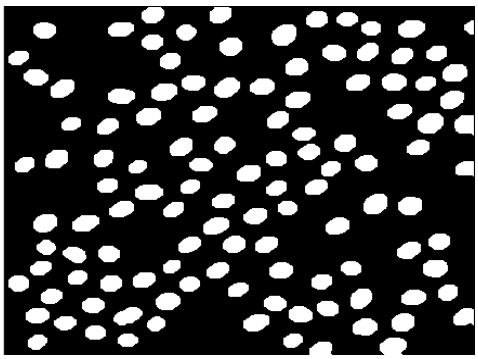

(f)

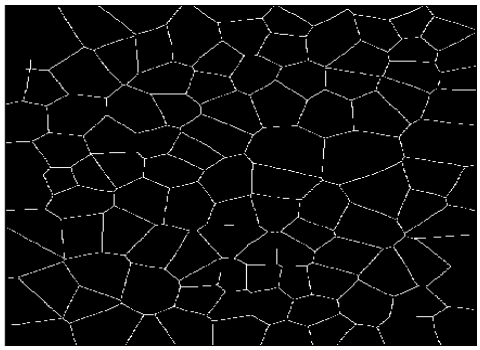

(g)

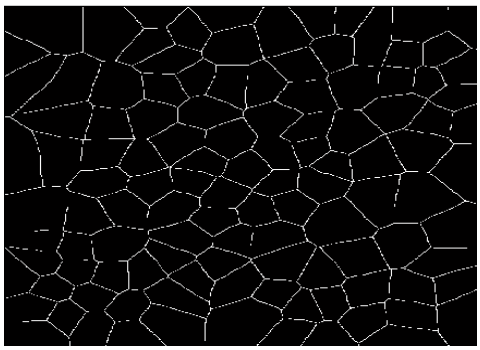

(h)

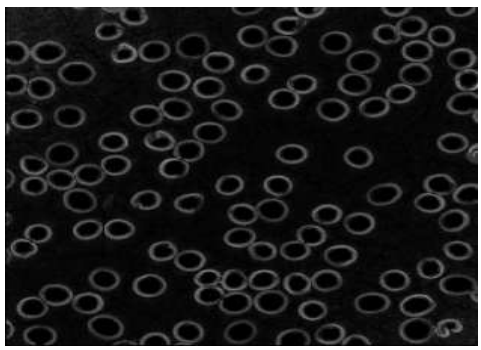

(i)

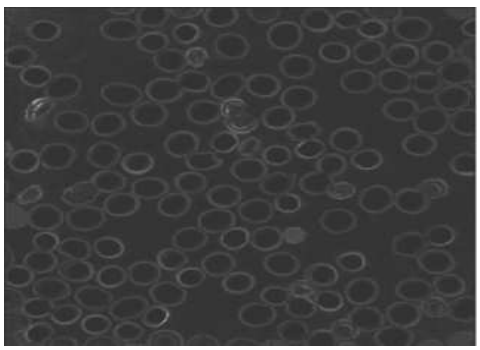

(j)

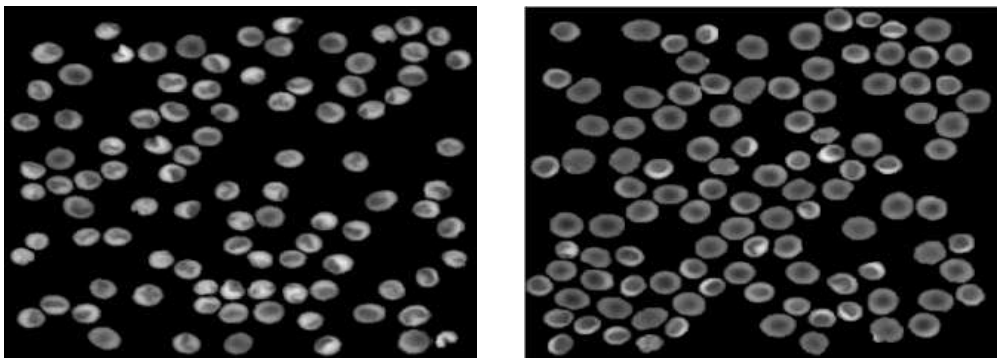

(k) (l)

Figure .14 Key steps of the proposed phase image segmentation.

where (a) and (b) are the newer and older RBCs phase images, (c) and (d) are the corresponding gradient images of original images, (e) and (f) are the internal markers, (g) and (h) are the external markers, (i) and (j) are the modified gradient images while (k) and (l) are the segmented phase images of newer and older RBCs, respectively.

Using this proposed method based on marker-controlled watershed, good experimental results for segmenting the RBCs phase images were obtained. It efficiently reduces the over-segmentation and under-segmentation. At the same time, it can separate the touched cells properly.

After successfully segmenting the phase image of RBCs via the method described in section 4, we can also get the inside and outside parts of the holographic phase image of RBCs respectively by using proposed method. Figure 15 is the segmentation result of the inside and outside parts of RBCs in Figure 14 (a) and (b).

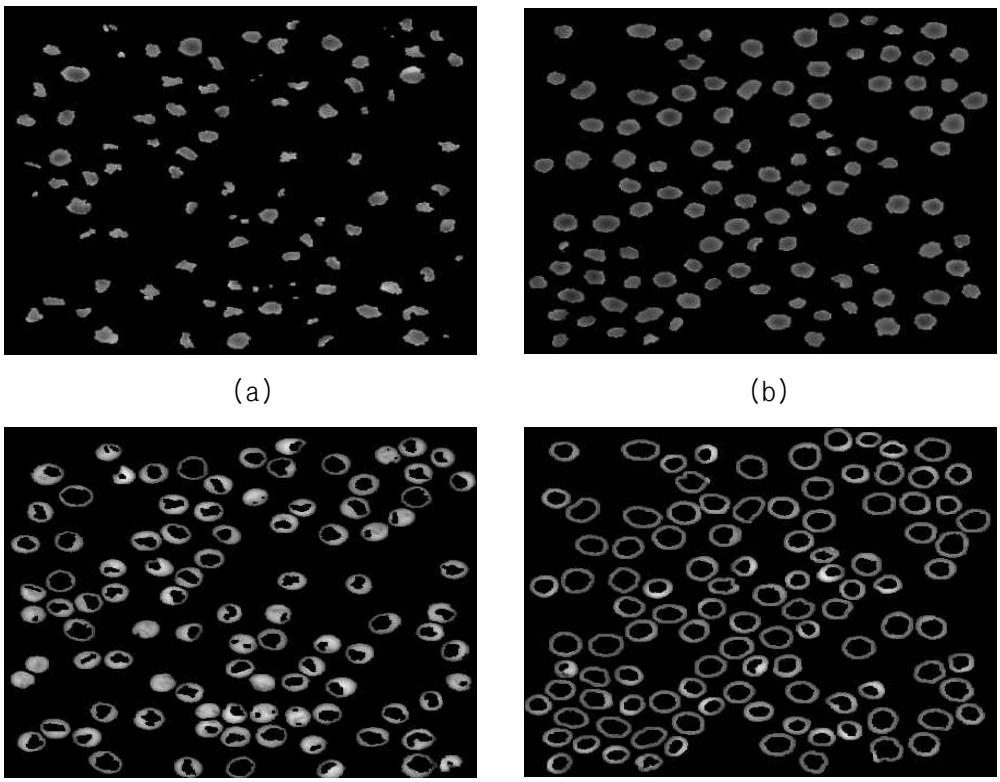

(a) (b)

(c) (d)

Figure 15. Segmentation results of the inside and outside parts of the RBCs phase image.

in figure 15, (a) and (b) are the inside part of the newer and older RBCs phase image while (c) and (d) are the outside part of the newer and older RBCs phase image.

5.2 Red Blood Cells Analysis Result

After segmentation, the mean phase value, area, dry mass and sphericity coefficient can be automatically calculated for every single RBC. Then, the joint statical distributions of these properties in RBCs are obtained for the statistical quantification of mean phase value, area, dry mass and

sphericity coefficient.

5.2.1 Mean Phase Value and Area

For the quantitative investigation of mean phase value and area of RBCs, two different storage periods RBCs are used. One kind of RBCs have 14 days storage times while the other one have 38 days storage times. The mean phase value and area for the inside parts of RBCs are also calculated. we use A part to denote the single RBC while B part to denote the inside part of RBCs as shown in Figure 16.

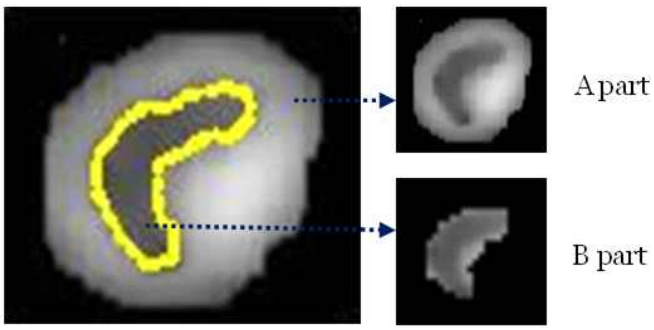

Figure 16. The schematic chart of different parts in red blood cells(RBCs)

Figure 17 shows the statistical distributions of the surface area and the mean of the phase value in the A part of a single RBC,respectively. Properties, which are surface area and mean phase value of single RBC in A part here, are considered as random variables and denoted as X_1 and X_2, respectively. As shown in Fig. 7, the mean and standard deviation of newer RBCs for variable X_1 are calculated to be 34 μm^2 and 5 μm^2, while they are 97° and 9° for random variable X_2. For older RBCs, the mean and standard deviation of variable X_1 are 42 μm^2 and 8 μm^2,while they are 74° and 15° for variable X_2, respectively. The standard deviations of random variable X_1 and X_2 in newer RBCs are smaller than those of older RBCs. This can be

explained that the single RBC in newer RBCs tends to be more similar than that in older RBCs since they are inclined to be much closer to the mean value. The mean of the phase value in the A part of the newer RBCs is larger than that in the older RBCs, while the mean of the surface area in the A part of newer RBCs is smaller than that of the older RBCs. It is noted that there was a difference of approximately 23° between the average phase values in the A part of the RBCs with different storage time. Also, it is noted that there was a difference of approximately $8\mu m^2$ betweenthe average surface areas values in the A part of the RBCs with different storage time. In addition, it is noted that the overlapped area between two statistical distributions of the phase value is smaller than that of the surface area.

Similarly, the surface area denoted as random variable X_3 and mean phase value as random variable X_4 for single RBC in the B part are used to analyze the distribution of the properties in newer and older RBCs. The mean and standard deviation of variable X_3 are calculated to be $10\mu m^2$ and 5 μm^2,while those of X_4 are 81° and 12° in newer RBCs. For older RBCs in B part, the mean and standard deviation of random variable X_3 are $18\mu m^2$ and 5 μm^2, while those of variable X_4 are 60° and 11°. The mean surface area in B part of newer RBCs is about $8\mu m^2$ smaller than that of older RBCs, while the standard deviation is very similar.

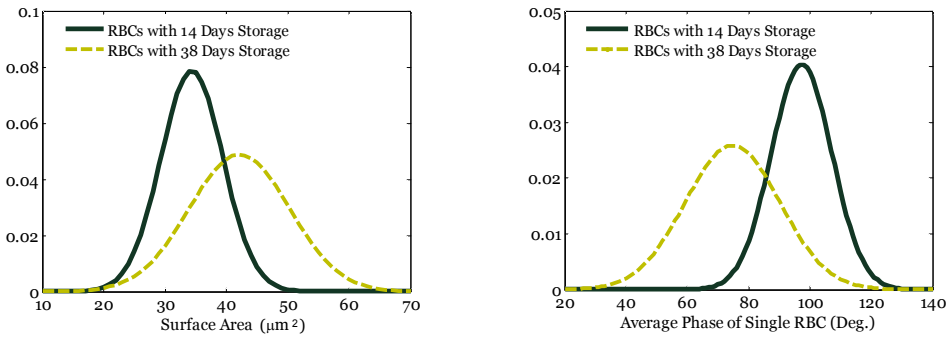

(a) (b)

Figure 17 statistical distribution of mean phase value and area of RBCs

in figure 17, (a) is the statistical distributions for the cell area in newer and older RBCs while (b) is the statistical distributions of the mean of phase value in part A [see Fig. 16] of RBCs. Newer RBCs have 14 days storage time and older RBCs have 38 days storage time.

Figure 18 shows a scatter plot of the relationship between the surface area and the mean of the phase value in A and B parts [see Fig. 4] in the RBC, respectively, where all single RBCs from the newer and older RBCs phase images were investigated. As shown in Fig. 18, it is noted that the surface area of the A or B parts of a single RBC is inversely proportional to the mean of the phase value in the A or B parts of both newer and older single RBCs. Further, it is noted that there is a strong correlation between the surface area and mean of the phase value in the A or B parts of both newer and older single RBCs. Also, Fig. 18 shows that there is a considerable separation between bivariate distributions or 3D morphology of the newer and older RBCs. In addition, it is noted that the mean of the phase value in the A or B parts of the newer RBCs is larger than that of older RBCs. However, the surface area in the A or B parts of the newer RBCs is smaller than that of older RBCs.

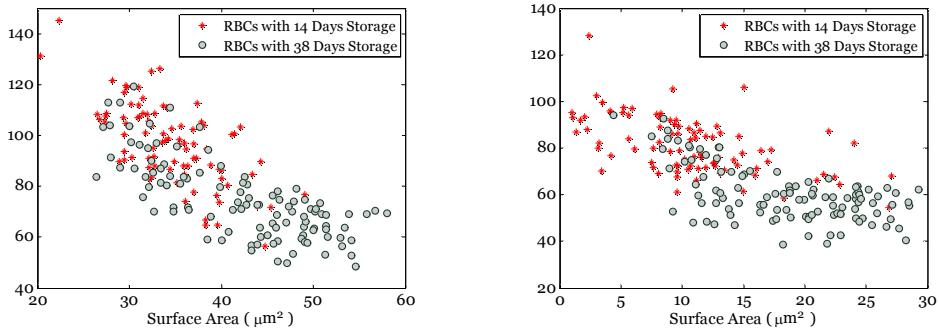

(a) (b)

Figure 18. A scatter plot of the relationship between the surface area and the mean of the phase value

in figure 18, (a) is the relationship bewteen surface area and mean phase value in A part while (b) is the relationship of that in B part [fig. 16].

5.2.2 Dry Mass

The dry mass of each RBChas been viewed as statistical population. The dry mass of single RBC in newer RBCs is denoted as random variable X_5, while in older RBCs it is represented as X_6. The mean and standard deviation of random variable X_5 are obtained to as 1788pg and 234pg, while those of X_6 are 1660pg and 234pg, respectively. Figure 19 shows the statistical distributions of the dry mass in the A part of a single RBC, where we have measured the dry mass of RBCs at different storage periods. It is noted that there was a difference of approximately 128 pg between the average dry mass values in the A part of RBCs with different storage periods. The dry mass of older RBCs is smaller than that of newer RBCs. From the above experimental results, we might conclude that this phenomenon result of any modifications of the hemoglobin concentration, since the dry mass basically depends on protein concentration and the dispersion of dry mass in both newer and older RBCs is very stable although the mean dry mass in newer RBCs is larger than

that in older RBCs.

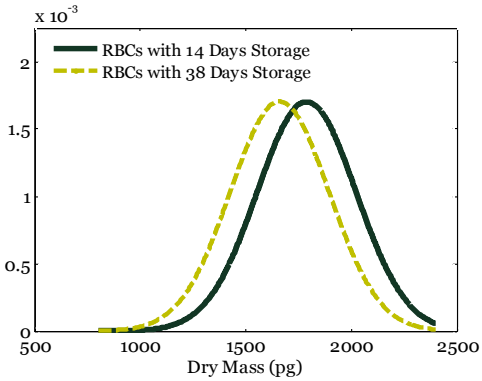

Figure 19. Statistical distributions of the dry mass in A part of RBCs

5.2.3 Sphericity Coefficient

The sphericity coefficient is taken as random variable while each single RBC can be serviced as sample data. X_7 and X_8 are used to denote random variable in newer and older RBCs. The mean and standard deviation for random variable X_7 in newer RBCs is calculated to be 0.54 and 0.21 while those values are 0.63 and 0.18 for random variable X_8 in older RBCs. Figure 20 is the statistical distribution for sphericity coefficient in newer and older RBCs by taking the samples' mean and standard deviation as population's mean and standard deviation (There are about 100 samples both in newer and older RBCs separately)

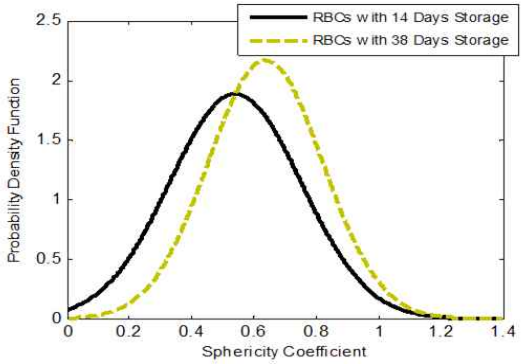

Figure 20. statistical distribution of sphericity coefficient in newer and older RBCs.

It is noted from Figure 20 that most of the sphericity coefficients in newer and older RBCs are smaller than 1 which means that most of the morphological types of single RBC are biconcave disk. When comparing the sphericity coefficient in newer RBCs with that in older RBCs, we can find that the average sphericity coefficient in older RBCs is bigger than that in newer ones, which can be explained that with the time gone, the morphological appearance of RBC tend to be much flatter without lesion since the RBCs with sphericity coefficient smaller than 1 occupy most parts in the whole RBCs population for a healthy person.

6. Conclusions

In this paper, we have presented a method to successfully segment the phase image of RBCs based on marker-controlled watershed. Advantages of the proposed method include reducing over-segmentation and under-segmentation. Furthermore, it can obtain the isolated RBC without touching other cells. Our automated RBCs segmentation algorithm enables one to adequately compare the different types of RBCs since the phase values in the background parts of the RBCs phase image can be set to 0° value. After segmentation by our method, we can automaticly calculate the RBCs's properties such as mean phase value, area, dry mass and sphericity coefficient. Thus, it is helpful for further studies on RBCs such as monitoring the change of 3D morphology, change of hemoglobin concentration and the classification or tracking of RBCs using the phase images obtained by digital holographic microscopy.

Reference

[1] B. Javidi, I. Moon, S.Yeom,andE.Carapezza, "Three-dimensional imaging and recognition of microorganism using single-exposure on-line (SEOL) digital holography," Opt. Express 13, 4492-4506, 2005.

[2] A. Stern and B. Javidi, "Theoretical analysis of three-dimensional imaging and recognition of microorganism technique using single-exposure on-line (SEOL) digital holography," J. Opt. Soc. Am. A 24, 163-168, 2007.

[3] I. Moon and B. Javidi, "3D identification of stem cells by computational holographic imaging,"J. R. Soc. Interface 4, 305-313, 2007.

[4] J. Laurie, D. Wyncoll, and C. Harrison, "New versus old blood - the debate continues,"Critical Care 14, 130, 2010.

[5] Colleen Gorman Koch, Liang Li, Daniel I. Sessler, Priscilla Figueroa, Gerald A. Hoeltge, Tomislav Mihaljevic, and Eugene H. Blackstone, "Duration of red-cell storage and complications after cardiac surgery,"New England Journal of Medicine 20, 1229-1239, 2008.

[6] J. W. Goodman and R. W. Lawrence, "Digital image formation from electronically detected holograms," Appl. Phy. Lett. 11, 77-79, 1967.

[7] I. Yamaguchi and T. Zhang,"Phase-shifting digital holography,"Opt. Lett. 22, 1268-1270,1997.

[8] T. Kreis, Handbook of Holographic Interferometry, NewYork,Wiley,2005.

[9] F. Dubois, L. Joannes, and J.-C. Legros,"Improved three-dimensional imaging with digital holography microscope using a partial spatial coherent source," Appl. Opt. 38, 7085-7094, 1999.

[10] T. Nomura, S. Murata, E.Nitanai,andT.Numata,"Phase-shifting digital holography with a phase difference between orthogonal polarizations," Appl. Opt. 45, 4873-4877, 2006.

[11] Y. Frauel, T. Naughton, O. Matoba, E. Tahajuerce, and B. Javidi,"Three dimensional imaging and display using computational holographic imaging,"Proc. of IEEE 94, 636-654, 2006

[12] E. Cuche, P. Marquet, and C. Depeursinge, "Spatial filtering for zero-order and twin-image elimination in digital off-axis holography,"Appl. Opt. 39, 4070-4075, 2000.

[13] Y. Zhang, G. Pedrini, W. Osten, and H. J. Tiziani, "Reconstruction of in-line digital holograms from two intensity measurements," Opt. Lett. 29, 1787-1789, 2004.

[14] P. Ferraro, S. De Nicola, G. Coppola, A. Finizio, D. Alfieri, and G. Pierattini, "Controlling image size as a function of distance and wavelength in Fresnel-transform reconstruction of digital holograms," Opt. Lett. 29, 854-856, 2004.

[15] D. Kim and B. Javidi, "Distortion-tolerant 3-D object recognition by using single exposure on-axis digital holography," Opt. Express 12, 5539-5548, 2005.

[16] E. Tajahuerce, O. Matoba, and B. Javidi, "Shift-invariant three dimensional object recognition by means of digital holography," Appl. Opt. 40, 3877-3886, 2001.

[17] B. Javidi and E.Tajahuerce, "Three dimensional object recognition using digital holography," Opt. Lett. 25, 610-612, 2000.

[18] T. Nomura, B. Javidi, S. Murata, E. Nitanai, and T. Numata, "Polarization imaging of a three-dimensional object by use of on-axis phase-shifting digital holography,"Opt. Lett. 32,481-483,2007.

[19] L. Martinez and B. Javidi, "Synthetic aperture single-exposure on-axis digital holography,"Opt. Express 16,161-169,2008.

[20] R.C. Gonzalez and R.E. Woods,Digital Imaging Processing, Prentice Hall, NewYork,NY,2002.

[21] P. Marquet, B. Rappaz, E. Cuche, T. Colomb, Y. Emery, C. Depeursinge and P. Magistretti,"Digital Holography microscopy: a non-invasive quantitative contrast

imaging technique allowing visualization of living cells," Optics Letters 30 468-470, 2005.

[22] E. Cuche, P. Marquet, and C. Depeursinge,"Simultaneous amplitude and quantitative phase contrast microscopy by numerical reconstruction of Fresnel off-axis holograms,"Appl. Opt. 38, 6994-7001,1999.

[23] T. Colomb, E. Cuche, F Charrière, J. Kühn, N. Aspert, P. Marquet, and C. Depeursinge,"Automatic procedure for aberration compensation in digital holographic microscopy and application to specimen shape compensation," Appl. Opt. 45, 851-863, 2006.

[24] B. Rappaz, E. Cano, T. Colomb, J. Kühn, C. Depeursinge, V. Simanis, P. Magistretti and P. Marquet, "Noninvasive characterization of the fission yeast cell cycle by monitoring dry mass with digital holographic microscopy", J. Biomed. Opt. 14, 034049, 2009.

[25] B. Rappaz, A Barbul, Y. Emery , R. Korenstein, C. Depeursinge, P. J. Magistretti, and P Marquet "Comparative study of human erythrocytes by digital Holographic microscopy, confocal microscopy and impedance volume analyzer," Cytometry Part A, 73, 895-903, 2008.

[26] P. Soille, Morphological Image Analysis: Principles and Application, 2nd ed., Springer-Verlag, NY,2003.

[27] X.Yang, H.Li and X.Zhou,"Nuclei segmentation using marker-controlled watershed, tracking using mean-shift and kalman filter in time-lapse microscopy," IEEE Trans on circuits and systems 53,2405-2414,2006.

[28] F.Meyer,"Topographic distance and watershed Lines," Signal Processing 38,113-125,1994

[29] C. Sun, X. Wang,"Spot segmentation and verification based on improve marker controlled watershed transform," International Conference on ICCSIT,63-66,2010.